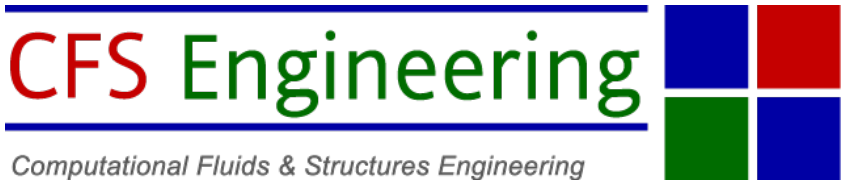

INTERNSHIP REPORT

June 9th 2025 – September 26th 2025

A Study of Thermo-Chemical Non-Equilibrium and Radiation in Hypersonic Re-entry Vehicles Using Computational Fluid Dynamics

APPLIED TO THE BSUV-2 TEST CASE

September 25, 2025

Author:

Justine Brun

Supervised by:

Jan Vos

Contents

Abstract

This report presents a numerical study of thermo-chemical non-equilibrium and radiative effects in hypersonic re-entry flows, focusing on the Bow-Shock Ultra-Violet 2 (BSUV-2) flight experiment conducted by the Innovative Science and Technology Office. The objective is to simulate and analyze the key physico-chemical processes occurring in the shock layer around a re-entry vehicle, using the NSMB (Navier–Stokes Multi-Block) solver with multi-species, multi-temperature air models.

Simulations were performed using both two- and three-dimensional configurations, across altitudes of 76.4 km and 71 km, using 11-species air models with varying chemical kinetics. The results are compared with reference flight data and other computational models to assess the accuracy of different modeling strategies. Emphasis is placed on predicting stagnation-line temperature profiles, mass and number density distributions, and the influence of different thermochemical models.

This work highlights the challenges of simulating hypersonic flow in transitional regimes. The BSUV-2 case provides a valuable validation benchmark for high-fidelity CFD tools used in high-altitude atmospheric entry analysis.

List of Figures

List of Tables

1 Introduction

The accurate prediction of hypersonic flow phenomena during atmospheric re-entry is crucial for the design and safe operation of spacecraft. One key challenge is modeling the complex thermo-chemical processes that govern the behavior of the shock layer formed around the vehicle.

Hypersonic flows at Mach numbers on the order of 20, typical of re-entry trajectories, result in extreme aerodynamic heating and strong shock waves. These conditions cause the atmospheric gas to dissociate and partially ionize in the shock-compressed layer near the vehicle surface. In addition to convective heating, significant radiative heat transfer can also occur, especially at high altitudes where the gas becomes optically thin. The intensity of these physico-chemical processes varies significantly with altitude.

This report focuses on the Bow-Shock Ultra-Violet (BSUV-2) flight experiment, developed by the Innovative Science and Technology Office of the Strategic Initiative Organization. The BSUV-2 mission provides valuable in-flight data on ultraviolet radiance and gas-surface interactions during hypersonic reentry at both low and high altitudes. The BSUV-2 dataset, which includes shock-layer UV emission spectra from species such as nitric oxide and atomic oxygen, serves as a key benchmark for validating computational tools that simulate non-equilibrium physico-chemical phenomena in hypersonic flows. The forward structure of the vehicle can be seen in Figure 1

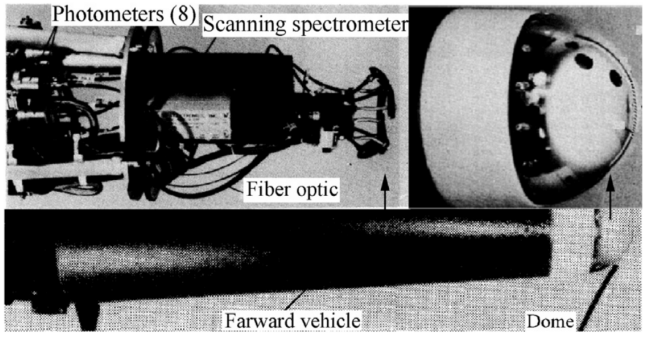

Figure 1: Forward structure of vehicle and instruments from [1]

The numerical methodology employed here involves solving the Navier–Stokes equations coupled with detailed thermo-chemical non-equilibrium models and (radiation transport). Various chemical kinetics are tested to assess their ability to reproduce the BSUV-2 flight observations, particularly along the stagnation region.

The objectives of this work include validating simulation results against other predictive models, with an emphasis on mass fractions and temperatures along the stagnation streamline. The report presents a detailed comparison of predicted flow characteristics over a range of altitudes, and discusses the implications for achieving reliable and accurate predictions of radiative and thermochemical behavior in hypersonic reentry environments.

2 BSUV-2 flight experiments

Two BSUV flight experiments were developed in the 1990s by the Innovative Science and Technology Office of the Strategic Initiative Organization to address key challenges related to hypersonic vehicles operating at both low and high altitudes. These experiments aimed to characterize the spectral distribution and intensity of ultraviolet radiation emitted from the bow-shock layer surrounding the vehicle's nose cone, as well as to study plume emissions from rocket motors, vehicle aerodynamics, and gas radiative noise affecting optical instrumentation.

The BSUV payload featured a half cone angle of 15° and a dome radius of 0.1016 m, housing several instruments including a scanning spectrometer, eight optical photometers, an electro-density microprobe, and two vacuum ultraviolet photometers. Figure 2 shows the arrangement of the instrumentation in the payload.

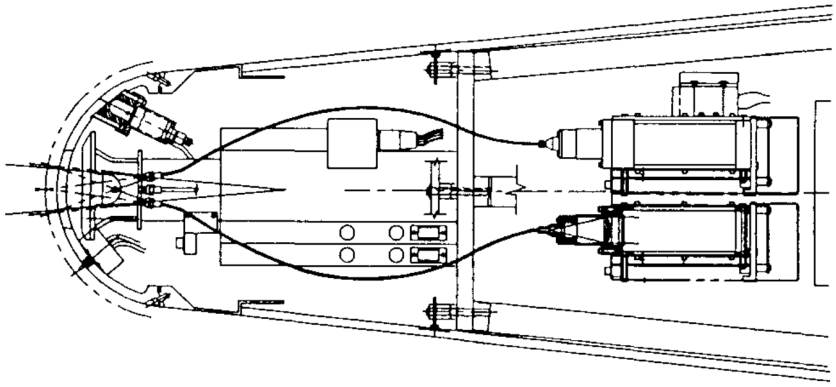

Figure 2: Schematic of instrument layout in the rocket payload from [2]

The experiments generated extensive ultraviolet spectral profiles of emissions within the bow-shock layer over altitude ranges of 38–70 km at approximately 3.5 km/s, and 100–65 km at about 5.1 km/s. These datasets serve as valuable benchmarks for validating computational models of radiative phenomena in hypersonic flow.

This work aims to simulate the BSUV-2 re-entry using the CFD code NSMB and to compare the results with those in the literature.

3 Simulation configuration

3.1 Geometry & meshing

The BSUV-2 vehicle was modeled using an axi-symmetric approximation, consistent with its geometry and the absence of angle of attack during the flight. This simplification reduces computational cost while preserving the essential physical features of the flow. A multi-block, structured mesh was used to discretize the flow domain. The mesh was designed to resolve the bow shock and the boundary layer with sufficient accuracy.

Figure 3 shows the axi-symmetic modeling of the BSUV-2 geometry, while Figure 4 provides an overview of the computational mesh used in the simulations.

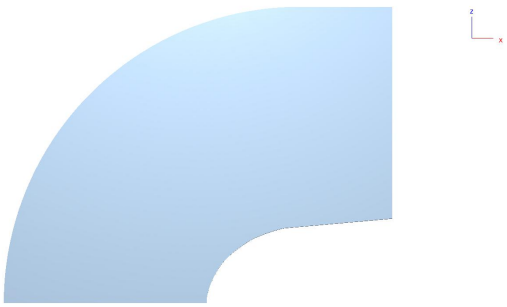

Figure 3: 2D modeling of the BSUV-2 geometry

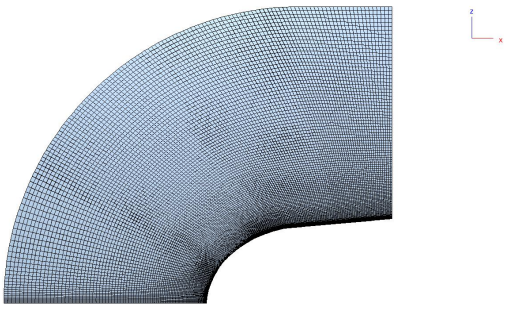

Figure 4: Overview of the 2D mesh

However, to address certain discontinuity issues that arose in the axisymmetric 2D mesh near the axis, a three-dimensional version of the vehicle was developed. This 3D model represented a quarter of the total geometry, exploiting symmetry, to improve numerical robustness and allow for more detailed resolution of flow features near the centerline. Figures 5 and 6 show the 3D geometry of the BSUV-2 vehicle and the corresponding computational mesh, respectively.

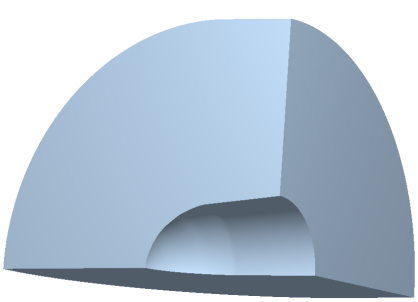

Figure 5: 3D modeling of the BSUV-2 geometry

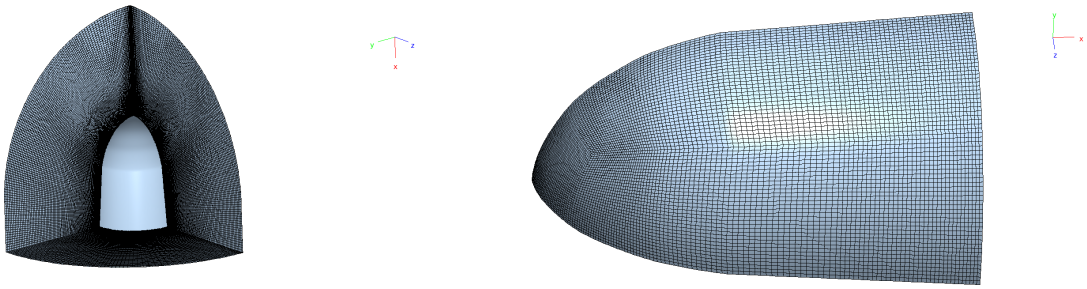

(a) Far-field mesh (b) Wall mesh

Figure 6: Overview of the 3D mesh

It should be noted that some discrepancies in the results compared to previous works may arise due to the lack of exact geometric coordinates for the vehicle. Since these coordinates were not provided for grid generation, the geometry was manually recorded from available diagrams, introducing a slight approximation in the model.

3.2 The NSMB solver

All CFD computations in this study were performed using the Navier–Stokes Multi Block (NSMB) solver, developed by a consortium of universities and industry partners [4]. NSMB is a parallelized, cell-centered finite volume solver designed for compressible flows on structured multi-block grids.

The code supports both explicit and implicit time integration schemes, with second- and fourth-order central discretizations (with artificial dissipation), as well as several upwind schemes up to fifth order. Turbulence modeling includes validated RANS models (up to 5 equations), LES, hybrid RANS–LES, and transition models.

NSMB was originally developed with hypersonic applications in mind, such as atmospheric re-entry. It includes various levels of chemical modeling for air, CO_2, and N_2, with available air models incorporating 5, 7, 11, or 13 species. Non-equilibrium models include those by Park (1989–2001), Gardiner, and Dunn–Kang, using equilibrium constants computed from polynomial fits (further details available in [4]).

Thermo-chemical non-equilibrium is modeled via the Landau–Teller theory for translational – vibrational energy exchange, with Millikan–White relaxation times. Transport coefficients are computed using the Blottner model or the Gupta-Yos model. Both inviscid and viscous flows (laminar and turbulent) are supported. Wall boundary conditions allow for super- and partially catalytic surfaces.

NSMB has been employed extensively in various European projects, demonstrating its versatility and robustness across a range of aerodynamic applications.

3.3 Numerical parameters

The simulations were carried out using the following numerical parameters. A total of 15 000 time steps (`NSTEPS`) were performed to advance the solution toward convergence.

For the three-dimensional model, the number of time steps was reduced to 7 000 to balance computational cost and accuracy. The Courant–Friedrichs–Lewy (CFL) number was set to 0.5 to ensure numerical stability. An implicit time integration scheme was employed, allowing for larger time steps and improved stability in capturing the flow features of hypersonic regimes.

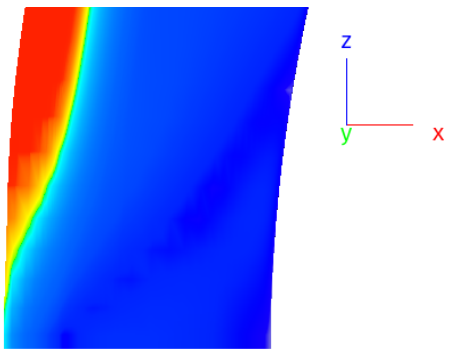

Figure 7: Carbuncle phenomenon at the vehicle forebody

Initially, a central differencing scheme was used for spatial discretization in combination with a standard artificial dissipation model. However, during the simulation, the carbuncle phenomenon emerged at the nose of the vehicle's forebody, resulting in a non-physical distortion of the bow shock along the stagnation line as seen in Figure 7.

It is important to note that this carbuncle phenomenon is a numerical artifact rather than a physical effect, as described by MacCormack [5]. This numerical instability manifests as a disruption ahead of the bow shock along the stagnation line. The instability is more likely to occur in high Mach number flows and becomes more severe when the computational grid is aligned with the shock front.

Hence, this issue necessitated a change in the numerical scheme. To mitigate the carbuncle instability, a second-order upwind AUSMDV (Advection Upstream Splitting Method – Diffusion and Velocity) and Van Leer hybrid scheme was adopted. This hybrid scheme offers enhanced robustness and accuracy in resolving strong shock waves and discontinuities. Its upwind nature helps reduce the shock misalignments that often trigger the carbuncle artifact.

Furthermore, to accurately capture shock waves and steep gradients, an `automatic` shock adaptation was performed in four successive stages for both models. The adaptation process is triggered when the shock is sufficiently well-defined, meaning it exhibits a strong gradient across adjacent cells. After completing these adaptation stages, the simulation was continued for an additional 5 000 steps to reach the final steady-state solution.

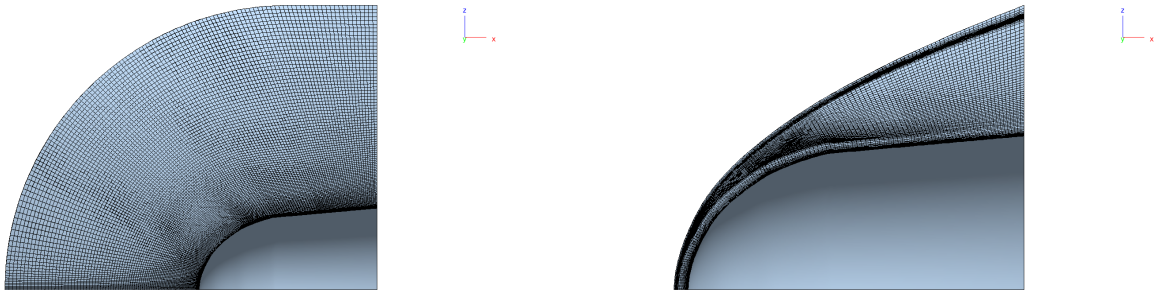

(a) Mesh without shock adaptation (b) Mesh after shock adaptation

Figure 8: Overview of the shock adaptation

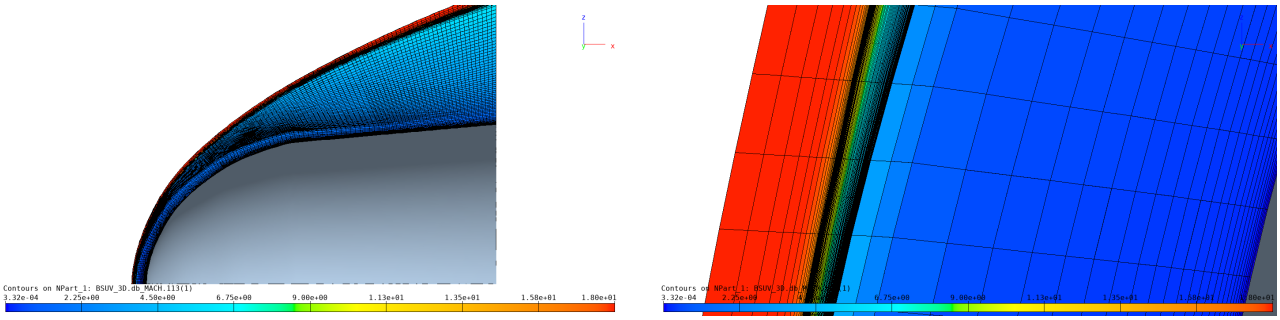

(a) Mesh after shock adaptation (b) Localized mesh refinement

Figure 9: Shock adaptation interface

Figures 8 and 9 illustrate the effect of the shock adaptation process on the computational mesh. Figure 8a shows the initial mesh before adaptation, while Figure 8b presents the refined mesh and grid bunching after shock adaptation. The corresponding Mach number distribution is shown in Figure 9a, and the localized mesh refinement near the shock is highlighted in Figure 9b.

3.4 Flow model

Although the Knudsen number is close to the continuum-transition threshold, the flow is still treated as a continuum. Specifically :

$$\mathrm{Kn} = \frac{\lambda}{L} \approx 0.0156 \quad \text{with} \quad \begin{cases} \lambda = 0.158 \cdot 10^{-2}\,\mathrm{m}\text{: mean free path} \\ L = R_n = 0.1016\,\mathrm{m}\text{: capsule's characteristic length} \end{cases}$$

This Knudsen number lies just above the commonly accepted continuum limit of $\mathrm{Kn} \approx 0.01$, but remains sufficiently low to justify the use of continuum-based CFD methods.

The simulations were conducted under the assumption of steady-state conditions. A laminar flow model was employed, appropriate for the flow regime under consideration. Viscous effects were modeled using the Blottner viscosity model with the Eucken correction to account for the thermal conductivity effects.

3.5 Kinetic model

The assumption of a quiescent, chemically frozen atmosphere at inflow is applied. The following assumptions are made at the inflow boundary:

- The air is considered a reacting gas mixture, composed of multiple species, including both neutral and ionized components.
- The inflow temperature and pressure are such that only the major neutral species (N_2, O_2) are present in significant amounts, while minor species and ionized components are initialized at trace concentrations.
- A specific air model with 7, 11 or 13 species is selected depending on the study carried out.

3.5.1 Chemical species

The chemical species considered are summarized in Table 1.

7 species	11 species	13 species
Molecular nitrogen (N_2)	Molecular nitrogen (N_2)	Molecular nitrogen (N_2)
Molecular oxygen (O_2)	Molecular oxygen (O_2)	Molecular oxygen (O_2)
Nitric oxide (NO)	Nitric oxide (NO)	Nitric oxide (NO)
Atomic nitrogen (N)	Atomic nitrogen (N)	Atomic nitrogen (N)
Atomic oxygen (O)	Atomic oxygen (O)	Atomic oxygen (O)
Electrons (e^-)	Ionized nitric oxide (NO^+)	Ionized nitric oxide (NO^+)
Ionized species	Ionized molecular nitrogen (N_2^+)	Ionized molecular nitrogen (N_2^+)
	Ionized molecular oxygen (O_2^+)	Ionized molecular oxygen (O_2^+)
	Atomic nitrogen ion (N^+)	Atomic nitrogen ion (N^+)
	Atomic oxygen ion (O^+)	Atomic oxygen ion (O^+)
	Electron (e^-)	Electron (e^-)
		Argon (Ar)
		Ionized argon (Ar^+)

Table 1: Chemical species considered in each air model (excluding the 5-species model)

3.5.2 Chemical reactions

In this work, we will primarily focus on the 11-species air model. Accordingly, the following reactions, including dissociation, recombination, ionization and charge exchange processes, are considered (as reported in [6]):

$$\mathrm{N_2 + M \rightleftharpoons 2N + M} \quad (1)$$
$$\mathrm{O_2 + M \rightleftharpoons 2O + M} \quad (2)$$
$$\mathrm{NO + M \rightleftharpoons N + O + M} \quad (3)$$
$$\mathrm{N_2 + O \rightleftharpoons NO + N} \quad (4)$$
$$\mathrm{NO + O \rightleftharpoons O_2 + N} \quad (5)$$
$$\mathrm{N + O \rightleftharpoons NO^+ + e^-} \quad (6)$$
$$\mathrm{N + N \rightleftharpoons N_2^+ + e^-} \quad (7)$$
$$\mathrm{O + O \rightleftharpoons O_2^+ + e^-} \quad (8)$$
$$\mathrm{N + e^- \rightleftharpoons N^+ + 2e^-} \quad (9)$$
$$\mathrm{O + e^- \rightleftharpoons O^+ + 2e^-} \quad (10)$$
$$\mathrm{N_2 + O_2^+ \rightleftharpoons N_2^+ + O_2} \quad (11)$$
$$\mathrm{NO^+ + N \rightleftharpoons O^+ + N_2} \quad (12)$$
$$\mathrm{NO^+ + O \rightleftharpoons N^+ + O_2} \quad (13)$$
$$\mathrm{NO^+ + O_2 \rightleftharpoons NO + O_2^+} \quad (14)$$
$$\mathrm{NO^+ + N \rightleftharpoons N_2^+ + O} \quad (15)$$
$$\mathrm{O_2^+ + N \rightleftharpoons N^+ + O_2} \quad (16)$$
$$\mathrm{O^+ + NO \rightleftharpoons NO^+ + O} \quad (17)$$
$$\mathrm{NO^+ + O \rightleftharpoons O_2^+ + N} \quad (18)$$
$$\mathrm{O^+ + N_2 \rightleftharpoons N_2^+ + O} \quad (19)$$

where M represents any species acting as a third body to conserve energy and momentum.

3.5.3 Mass fractions

We assume the atmosphere's air has the composition presented in Table 2, as mentioned previously.

Species	Mass fraction
$\mathrm{N_2}$	0.76536
$\mathrm{O_2}$	0.23464
N	1×10^{-12}
NO	1×10^{-12}
O	1×10^{-12}
$\mathrm{NO^+}$	1×10^{-12}
$\mathrm{N_2^+}$	1×10^{-12}
$\mathrm{O_2^+}$	1×10^{-12}
$\mathrm{N^+}$	1×10^{-12}
$\mathrm{O^+}$	1×10^{-12}
e^-	1×10^{-12}

Table 2: Initial mass fractions at the inflow boundary

3.6 Thermo-chemical models

The kinetic model employed in this study accounts for thermo-chemical non-equilibrium effects, typical of hypersonic flow environments. These effects arise at high speeds and altitudes when the characteristic flow time around a hypersonic vehicle is comparable to or shorter than the time required for molecular collisions to restore equilibrium. Chemical non-equilibrium effects are captured using `gas model 4`, while thermo-chemical non-equilibrium, where both chemical kinetics and internal energy mode relaxation are treated in a coupled manner, is modeled using `gas model 5`.

To model the vibrational relaxation behavior of diatomic molecules, Millikan-White's empirical model was considered for the vibrational relaxation time.

3.7 Boundary conditions

The inflow boundary conditions correspond to the free-stream experimental data reported in [6] and [1] at $h = 76.4\,\text{km}$. The wall temperature is fixed at $T_{\text{wall}} = 1\,000\,\text{K}$. The surface is considered non-catalytic. Additionally, thermal equilibrium between the vibrational and wall temperatures is assumed at the streamlined surface, i.e. $T_{\text{vib}} = T_{\text{wall}}$. Ablation is not considered here.

3.8 Conditions for BSUV-2 test cases

Table 3 presents the initial data for the numerical modeling as described in [6]. All input files were initialized using these conditions.

Altitude (km)	$\mathbf{u_\infty}$ **(km/s)**	**Mach**	$\mathbf{T_\infty}$ **(K)**	ρ_∞ **(kg/m^3)**
76.4	5.1	18	206	$5.14 \cdot 10^{-5}$
71	5.1	17.2	216.85	$7.2 \cdot 10^{-5}$

Table 3: Conditions for BSUV-2 test case

It should be noted that the reference curves used from the literature used later on in this report were not available in electronic format and were therefore digitized manually. As a result, some uncertainty and limited precision should be considered when interpreting these comparisons.

4 Numerical simulation results at h = 76.4 km

The flow field is simulated using NSMB with different thermo-chemical models and the results are compared to previous investigations by [6] in terms of temperature and species mass fractions.

4.1 Flow property contours along the capsule skin

The results presented in Figures 10, 11, and 12 were obtained from flow simulations using an 11-species air model based on Park's 1993 chemical non-equilibrium model. The temperature and pressure distributions show overall agreement between the 2D and 3D results, while Figures 11a and 11b highlight the strong shockwave that forms ahead of the capsule's forebody in both 2D and 3D configurations. The boundary layer remains relatively thin due to the intermediate flight speed of the BSUV-2 vehicle.

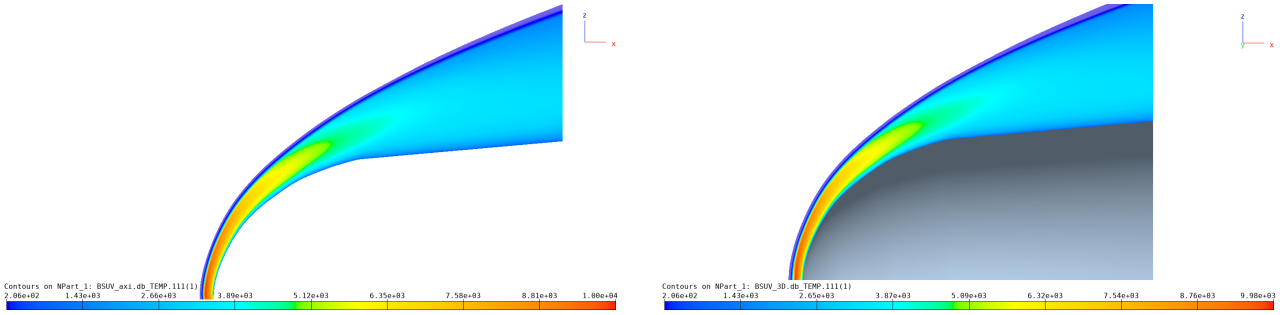

(a) 2D (b) 3D

Figure 10: Temperature contours obtained with Park's 1993 non-equilibrium chemistry model for the 11-species air model

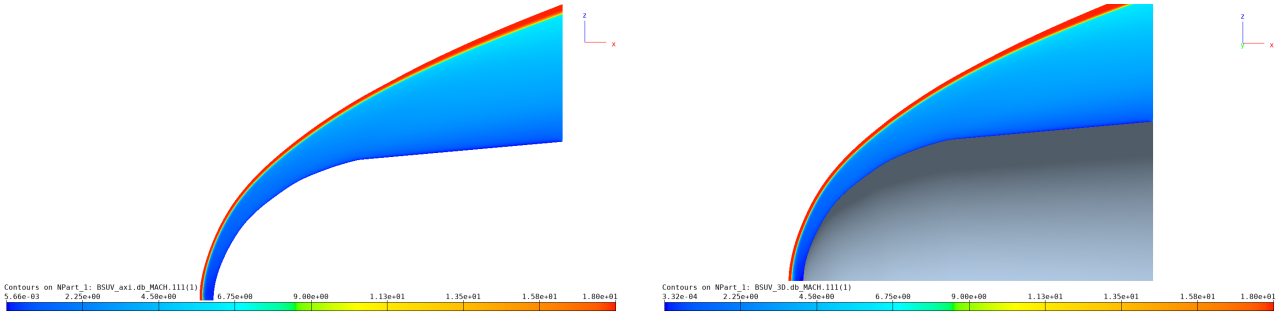

(a) 2D (b) 3D

Figure 11: Mach number contours obtained with Park's 1993 non-equilibrium chemistry model for the 11-species air model

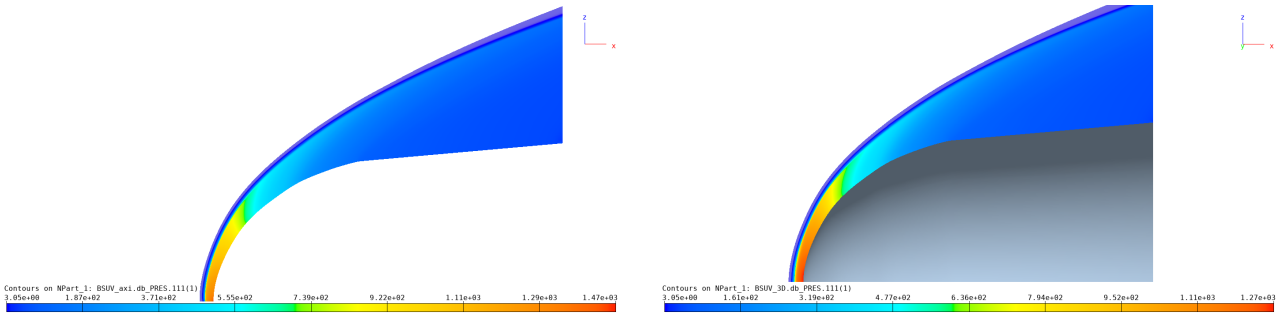

(a) 2D (b) 3D

Figure 12: Pressure contours obtained with Park's 1993 non-equilibrium chemistry model for the 11-species air model

Similar contours are observed for other configuration models, with only minor variations in the values and slight differences in the shock layer thickness.

4.2 Temperature distributions along the stagnation streamline

The chemical non-equilibrium and thermo-chemical non-equilibrium models predict slightly different temperature gradients and, particularly, the former tends to underestimate the translational temperatures compared to [6]'s results as seen in Figure 13. The cause of this discrepancy is probably due to the different thermo-chemical models used for the simulation.

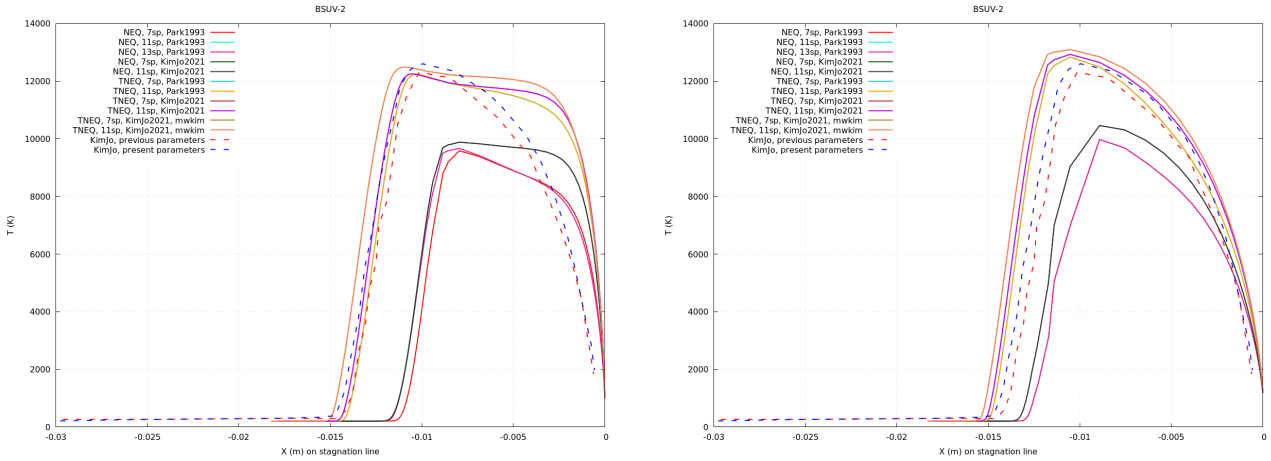

(a) 2D (b) 3D

Figure 13: Translational temperature profiles along the stagnation line

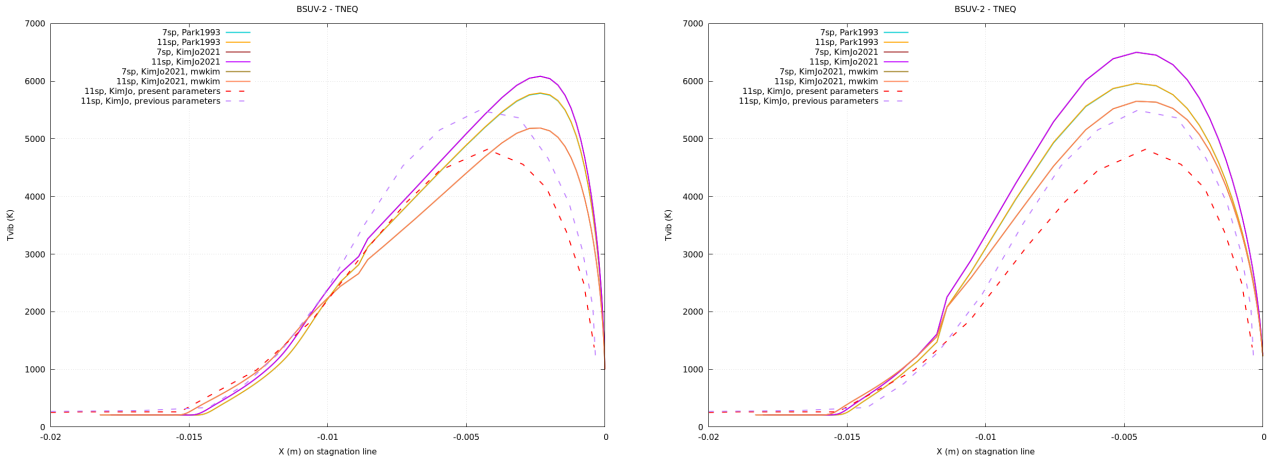

(a) 2D (b) 3D

Figure 14: Vibrational temperature profiles along the stagnation line

The shock positions shown in both the 2D (Figure 13a, Figure 14a) and 3D (Figure 13b, Figure 14b) thermo-chemical non-equilibrium, 11-species air model results match well with those from [6], with the 3D model showing even better agreement with Kim's calculations.

The vibrational temperature profiles of Figure 14 exhibit good agreement across all models. The NSMB simulations show slightly higher vibrational temperature values, but the overall profile shape and behavior remain similar, with only minor variations.

4.3 Mass fraction distributions along the stagnation streamline

The mass fraction distributions of key species, i.e. nitric oxide (NO), atomic oxygen (O), and molecular oxygen (O_2), were evaluated along the stagnation streamline and are presented in Figure 15. The results are shown for both the 2D and 3D configurations using an 11-species air model and are compared against the reference data from KimJo [6].

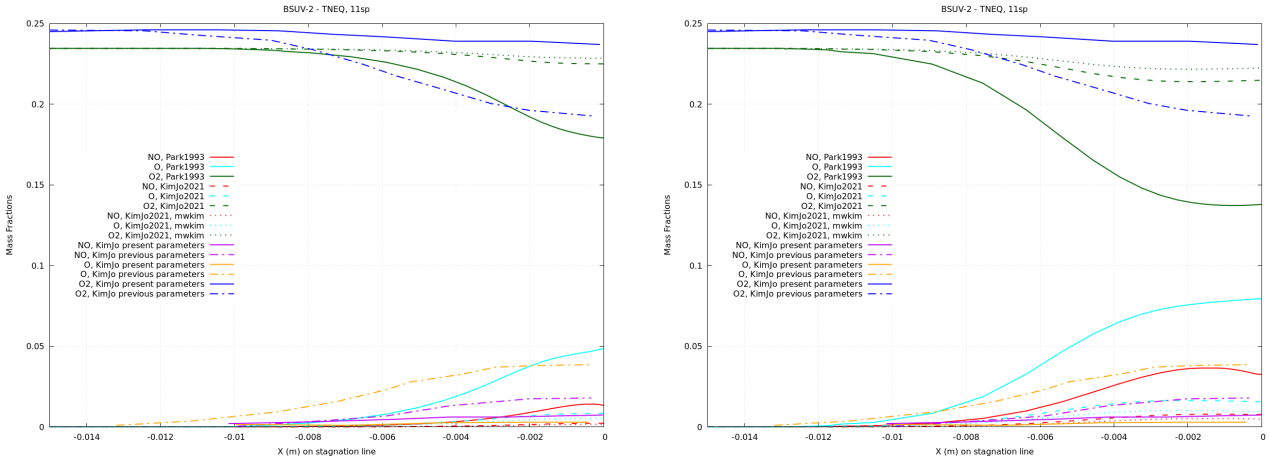

(a) 2D (b) 3D

Figure 15: Mass fraction distributions along the surface for 11-species air model

The curves corresponding to Kim's previous parameters predict significantly higher peak values for NO (purple dash-dot) and O (yellow dash-dot) compared to the present paramaters and 2D models (Figure 15a). This indicates a strong degree of dissociation and reactivity, particularly in the post-shock region. The molecular oxygen (O_2 in dark green) fraction shows a sharp decline upstream, indicating fast dissociation rates particularly for the 3D case (Figure 15b).

Comparing the two cases, the trends of the results remain consistent in terms of species ordering and relative magnitudes, but the steepness of the curves are different. The 2D simulations show less abrupt thermal-chemical transitions and weaker gradients upstream, which may understate dissociation and reaction zones due to geometric constraints. The 3D model produces smoother distributions along the entirety of the stagnation streamline that are more representative of realistic flow behavior. Overall, the 3D results indicate slightly higher dissociation and NO formation near the stagnation point, reflecting a more prominent shock structure and chemical response.

Furthermore, the comparison between Kim's present and previous parameters reveals that the older parameter set consistently predicts higher levels of the three chemical entities under study. According to [6], this is attributed to the use of higher O_2 dissociation rates in the older model, which enhance the availability of atomic oxygen in the shock layer. As documented in Kim's analysis, these earlier dissociation rates significantly overpredict dissociation in $O_2 + O_2$, $O_2 + O$, and $O_2 + N_2$ collisions relative to reference shock-tube data. The updated parameters mitigate this overprediction by incorporating refined rate constants based on more recent experimental and state-resolved kinetic data.

4.4 Electron number density along the stagnation streamline

Additionally, Figure 16 shows the electron number density along the stagnation streamline.

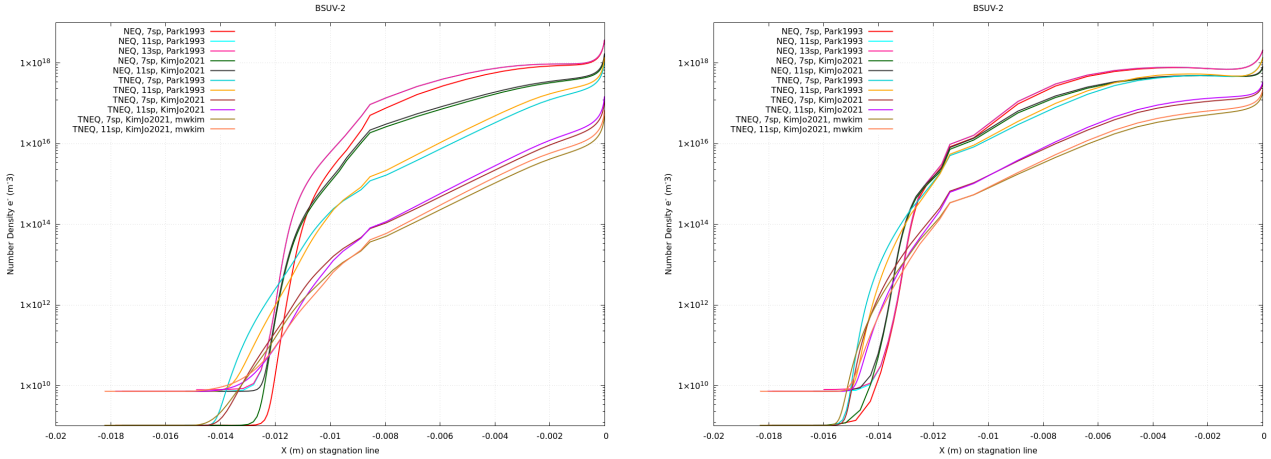

(a) 2D (b) 3D

Figure 16: Electron number density profiles along the stagnation streamline

Although no reference data is available for validation, only minor differences are observed between the 2D (16a) and 3D (16b) simulations. Notably, the location where the density gradient increases sharply occurs slightly earlier in the 3D case. Additionally, slight variations appear near $X = -0.012\,\mathrm{m}$ with notable "bumps" seen in Figure 16b. Overall, the values remain close, particularly at the peak near the stagnation point.

5 Numerical simulation results at h = 71 km

Following the approach used at 76.4 km, simulations are now performed at 71 km using the same thermo-chemical models. Results are compared with reference data from Niu [1] and Candler [7] to evaluate model performance at this lower altitude.

5.1 Temperature distributions along the stagnation streamline

Figure 17a shows the translational temperature profiles along the stagnation streamline. The shock location predicted by the NSMB models aligns well with Candler's CFD simulation [7], although it yields a slightly higher peak temperature. In contrast, the DSMC model and the results reported by Niu [1] predict lower temperatures and position the shock closer to the forebody of BSUV-2.

Similarly, Figure 17b presents the vibrational temperature distribution. Once again, the NSMB models show the best agreement with Candler's CFD [7], with Kim & Jo's 2021 chemical model predicting the highest peak. Niu's CFD [1] results remain consistent with respect to the peak location, closely matching the NSMB predictions. Meanwhile, the DSMC data from Candler exhibit a slightly forward-shifted peak, mirroring the trend previously observed in the translational temperatures.

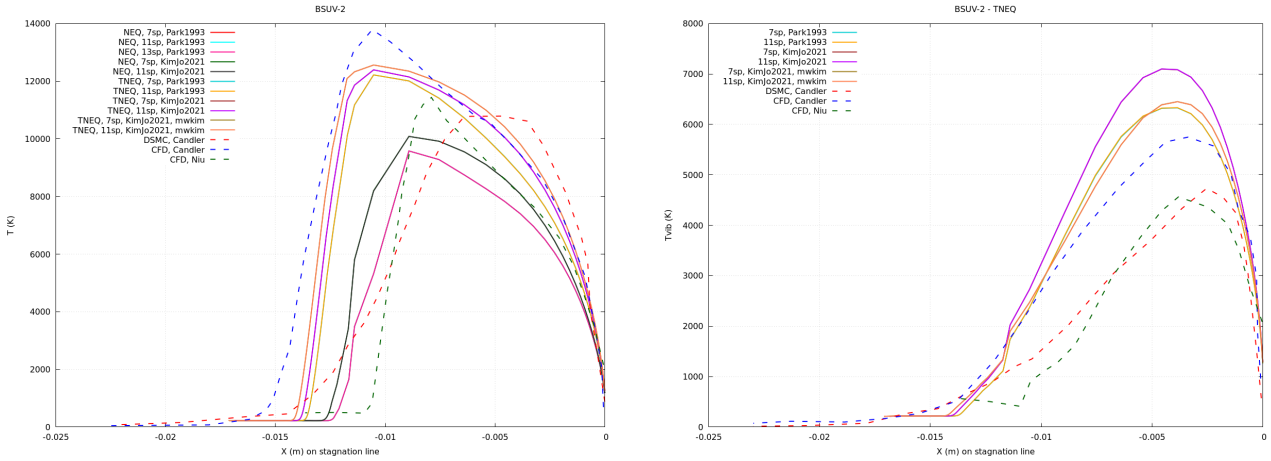

(a) Translational (b) Vibrational

Figure 17: Temperature profiles along the stagnation line

5.2 Number density distributions along the stagnation streamline

The number density of key species, i.e. atomic nitrogen (N), atomic oxygen (O) and nitric oxide (NO), was evaluated along the stagnation streamline. The following expression was used to compute the number density N_i of species i:

$$N_i = \frac{w_i \cdot \rho}{M_i} \cdot N_A \quad \text{with} \quad \begin{cases} w_i : \text{mass fraction of species } i \\ \rho : \text{mixture density} \\ M_i : \text{molar mass of species } i \\ N_A : \text{Avogadro's number} \end{cases}$$

The results highlight varying levels of agreement between the selected thermochemical models and the reference Candler DSMC and CFD datasets.

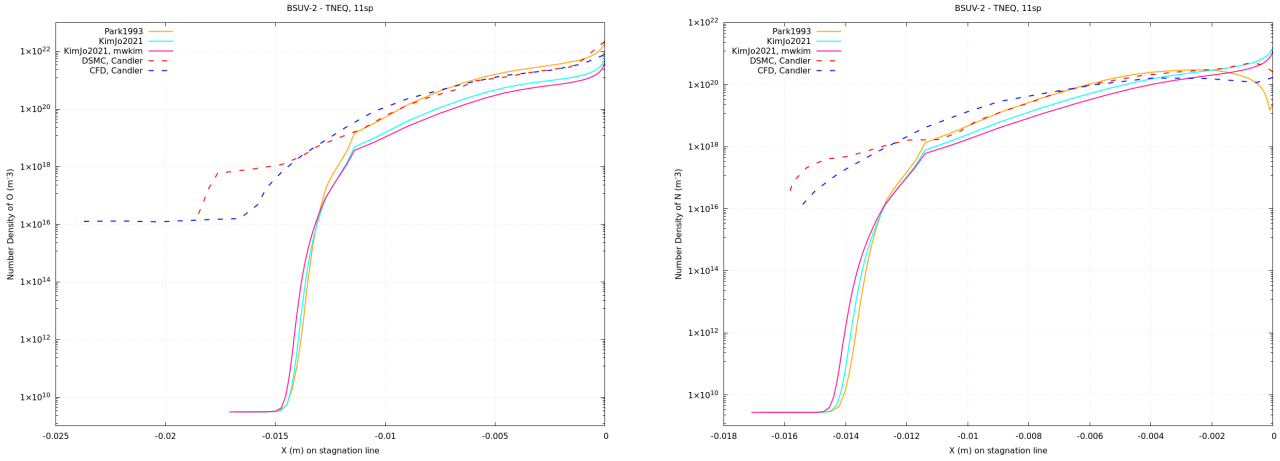

(a) Atomic oxygen (O) (b) Atomic nitrogen (N)

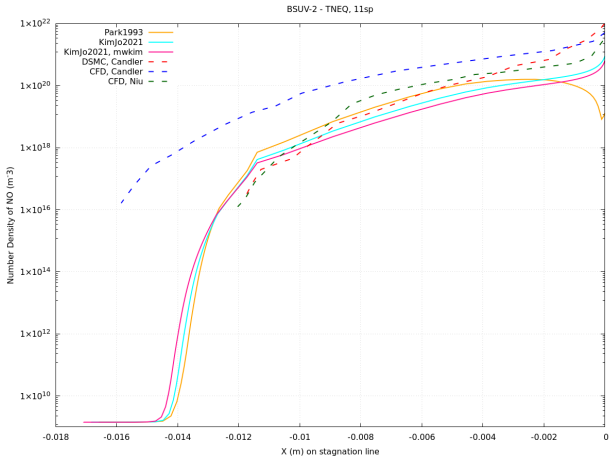

(c) Nitric oxide (NO)

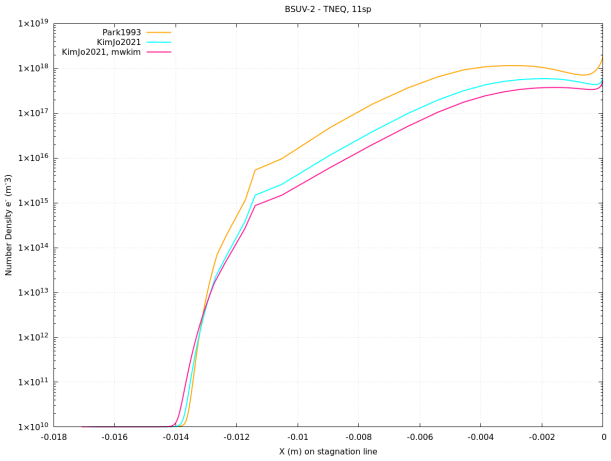

(d) Electrons (e^-)

Figure 18: Number density profiles along the stagnation streamline

Park's 1993 model shows the best agreement with DSMC and CFD data throughout the post-shock region in Figure 18a. Kim & Jo's 2021 model slightly underpredicts O densities near the wall, likely due to differences in dissociation rates or vibrational non-equilibrium effects.

For atomic nitrogen (Figure 18b), all models capture the general trend; however, the Park 1993 model and the Kim & Jo 2021 model using the Millikan-White Kim approach for vibrational relaxation show better agreement with both DSMC and CFD predictions in the post-shock region. The observed decrease in nitrogen density near the stagnation point follows the trend predicted by Candler's CFD results, though the magnitude is notably lower.

Considerable deviations are observed in Figure 18c, particularly with respect to the CFD data from Candler, which predict significantly higher NO concentrations. All models underpredict NO density, indicating that rate constants may not be accurately captured under the applied modeling assumptions.

Moreover, the electron number density distribution is shown in Figure 18d; however, no reference data is available for direct comparison. Overall, both the distribution trends and the magnitude of the values are consistent with those obtained at a different altitude in previous simulations.

6 Conclusions

The numerical investigation of the BSUV-2 reentry case demonstrates that thermo-chemical non-equilibrium modeling is essential for accurately simulating high-altitude hypersonic flows. Using the NSMB solver and 11-species air models, simulations reproduced key physical behaviors observed in flight, particularly in terms of shock-layer structure, species dissociation, and vibrational energy modes.

Comparisons between two- and three-dimensional results show that 3D simulations offer smoother profiles and better alignment with reference data, especially for species mass fractions and post-shock dissociation levels. Additionally, at the altitudes under study, the flow enters a transitional regime where non-equilibrium effects become more pronounced and continuum-based CFD begins to lose predictive accuracy.

A comparative analysis with DSMC and CFD data from the literature shows that while NSMB-based CFD simulations capture overall trends effectively, they tend to underpredict number densities in some cases, especially for nitric oxide. This highlights the limitations of continuum assumptions in rarefied regimes, where DSMC provides a more accurate molecular-level representation.

Overall, the results emphasize the importance of choosing the appropriate modeling approach based on the flight regime. For high-altitude applications where rarefied gas dynamics play a significant role, hybrid strategies combining continuum CFD and particle-based DSMC methods may provide the best predictive capabilities. The BSUV-2 test case continues to serve as a valuable benchmark for advancing numerical tools in the study of hypersonic non-equilibrium flows.

References

[1] Niu Q., Liu X., Li Y., Zhang S., *Prediction of shock-layer ultraviolet radiation for hypersonic vehicles in near space*, Chinese Journal of Aeronautics, 2016. DOI: 10.1016/j.cja.2016.04.021

[2] Erdman P. W., Zipf E. C., Espy P., Howlett C., Levin D. A., Loda R., Collins R. J., Candler G. V., *Flight measurements of low-velocity bow shock ultraviolet radiation*, Journal of Thermophysics and Heat Transfer, 1993. DOI: 10.2514/3.11566

[3] Erdman P. W., Zipf E. C., Espy P., Howlett C. L., Levin D. A., Collins R. J., Candler G. V., *Measurements of ultraviolet radiation from a 5-km/s bow shock*, Journal of Thermophysics and Heat Transfer, 2012. DOI: 10.2514/3.562

[4] Hoarau Y., Pena D., Vos J. B., Charbonnier D., Gehri A., Braza M., Deloze T., Laurendeau E., *Recent developments of the Navier-Stokes Multi Block (NSMB) CFD solver*, AIAA SciTech 2016, 4–8 Jan, San Diego, CA. DOI: 10.2514/6.2016-2056

[5] MacCormack R. W., *The Carbuncle CFD Problem*, 49th AIAA Aerospace Sciences Meeting including the New Horizons Forum and Aerospace Exposition, 4–7 January, Orlando, Florida. AIAA 2011-381. DOI: 10.2514/6.2011-381

[6] Kim J. G., Jo S. M., *Modification of chemical-kinetic parameters for 11-air species in re-entry flows*, International Journal of Heat and Mass Transfer, vol. 173, 2021, Article 121221. DOI: 10.1016/j.ijheatmasstransfer.2021.121221

[7] Candler G., Boyd I., Levin D., Moreau S., Erdman P., *Continuum and DSMC Analysis of Bow Shock Flight Experiments*, AIAA Paper 93-0275, 31st Aerospace Sciences Meeting & Exhibit, Reno, NV, 11–14 Jan, 1993.